REAL-TIME, LASER-BASED SENSORS FOR MILITARY AND CIVILIAN APPLICATIONS

Rosario C. Sausa*
U.S. Army Research Laboratory
AMSRD-ARL-WM-BD
Aberdeen Proving Ground, MD 21005-5066

Jerry Cabalo
GeoCenters
US Army Edgewood Chemical Biological Center
Aberdeen Proving ground, MD 21010

ABSTRACT

We report on a novel laser-based technique coined surface laser photofragmentation-fragment detection (SPF-FD) spectroscopy for detecting explosives residues, chemical warfare agents, and other hazardous materials on surfaces in real time at ambient conditions. Our technique utilizes one or two lasers to both photolyze the target species and to facilitate the detection of the characteristic photofragments by resonance-enhanced multiphoton ionization, laser induced fluorescence, or both. We demonstrate its analytical utility on explosives RDX, HMX, CL20, and TNT, and report the effects of laser photofragmentation wavelength and energy, delay between photofragmentation and probe lasers, and electrode orientation on signal intensity. Signal to noise analyses yield limits of detection in the range of 1 to 15 ng/cm^2 (S/N=3) at 1 atm and 298K.

1. INTRODUCTION

The Detection and monitoring of explosives residues is critical to the safety and security of our warfighters and general population. It is of particular interest in the areas of detecting potential terrorist activity, demilitarization, and minesweeping operations. As a result of interest in these areas, we have developed an advanced laser-based sensor to reduce the risk to the warfighter and general population by detecting the presence of these materials and preventing their use. A photograph of our prototype sensor head is shown in figure 1.

Our sensor offers the combination of high sensitivity and selectivity with real-time monitoring capabilities, and is based on surface laser photofragmentation (SPF) with subsequent fragment detection (FD). It utilizes one or two lasers to photofragment the analyte species and to facilitate the detection of the characteristic photofragments by resonance - enhanced multiphoton ionization

Fig. 1. Photograph of hand-held, laser probe.

(REMPI), laser-induced fluorescence (LIF), or both. This approach is particularly desirable for explosives with low vapor pressures at ambient conditions that cannot be detected in the gas-phase and explosives which do not lend themselves to direct spectroscopic detection because they posses weak transitions or broad and poorly defined spectral features. SPF results in the formation of small, characteristic fragments (e.g. monatomic, diatomic and triatomic species) that can be detected by the above-mentioned methods due to a favorable combination of usually strong optical transitions and sharp, well-resolved spectral features. Since the fragments are characteristic of the chemical composition of the precursor molecule, they also contribute to the selectivity of the method. One important feature of the SPF-FD method is its utility for detecting of classes of compounds. When molecules share a common functionality (e.g. NO_2 for explosives, PO for organophosphonates, As for arsenic-containing compounds, or F, Cl, and Br for halogenated compounds) the functionality may be targeted for fragmentation and detection (see figure 2).

Report Documentation Page

Form Approved
OMB No. 0704-0188

1. REPORT DATE	2. REPORT TYPE	3. DATES COVERED
00 DEC 2004	**N/A**	**-**

4. TITLE AND SUBTITLE	5a. CONTRACT NUMBER
Real-Time, Laser-Based Sensors for Military and Civilian Applications	5b. GRANT NUMBER
	5c. PROGRAM ELEMENT NUMBER
6. AUTHOR(S)	5d. PROJECT NUMBER
	5e. TASK NUMBER
	5f. WORK UNIT NUMBER
7. PERFORMING ORGANIZATION NAME(S) AND ADDRESS(ES) **U.S. Army Research Laboratory AMSRD-ARL-WM-BD Aberdeen Proving Ground, Md 21005-5066; GEO Center US Army Edgewood Proving Ground, MD 21010**	8. PERFORMING ORGANIZATION REPORT NUMBER
9. SPONSORING/MONITORING AGENCY NAME(S) AND ADDRESS(ES)	10. SPONSOR/MONITOR'S ACRONYM(S)
	11. SPONSOR/MONITOR'S REPORT NUMBER(S)

12. DISTRIBUTION/AVAILABILITY STATEMENT
Approved for public release, distribution unlimited

13. SUPPLEMENTARY NOTES
See also ADM001736, Proceedings for the Army Science Conference (24th) Held on 29 November - 2 December 2004 in Orlando, Florida., The original document contains color images.

14. ABSTRACT

15. SUBJECT TERMS

16. SECURITY CLASSIFICATION OF:			17. LIMITATION OF ABSTRACT	18. NUMBER OF PAGES	19a. NAME OF RESPONSIBLE PERSON
a. REPORT **unclassified**	b. ABSTRACT **unclassified**	c. THIS PAGE **unclassified**	**UU**	**8**	

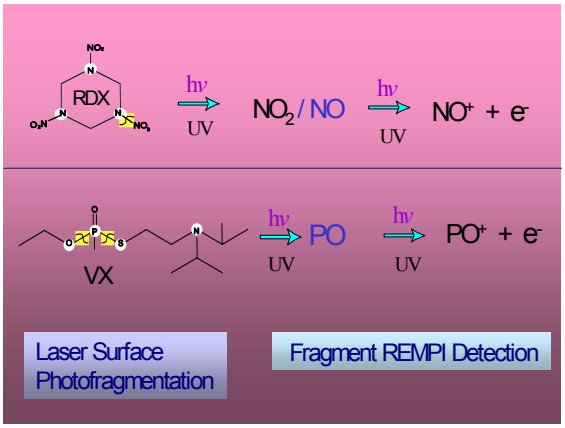

Fig. 2. SLP-FD approach for RDX and VX detection

Optimization of the technique for the detection of a characteristic fragment allows a class of compounds to be detected by a single spectroscopic approach.

In this paper, we report the detection of explosive residues RDX, HMX, CL20, and TNT in situ and in real time by SPF-FD spectroscopy. A laser operating in the ultraviolet photofragments RDX on a surface and a second laser tuned to 226 nm ionizes the characteristic NO fragment by means of its $A\Sigma^{+}$-$X\Pi$ (0,0) transitions by (1+1) REMPI. The NO fragment is characteristic of the NO_2 functional group that is present in these molecules. We report the effects of laser photofragmentation wavelength and energy, delay between photofragmentation and ionization lasers, and electrode configuration on signal intensity. We use an ion optics simulation program to model the electric field of two sets of electrodes in the presence of a substrate and reveal the more sensitive configuration. Signal-to-noise analyses yield detection limits in the low ng/cm^2 (S/N=3) at 1 atm and 298K.

2. SENSOR

Our previous publication contains the details of the SPF-FD technique (Cabalo and Sausa, 2003). An abridged description of the experimental apparatus follows Briefly, a laser beam excites a thin film of energetic material placed on the surface of a quartz plate, and second laser beam, whose frequency is in the 224- to 226-nm range ionizes the resulting NO photofragment by REMPI. We direct the excitation laser beam perpendicular to the substrate surface and the ionization laser beam parallel to the substrate surface. The pump and probe laser energies are in the 10 to 20 μJ range. A pulse generator (Stanford Research Systems, DG 535) controls the time delay between the lasers.

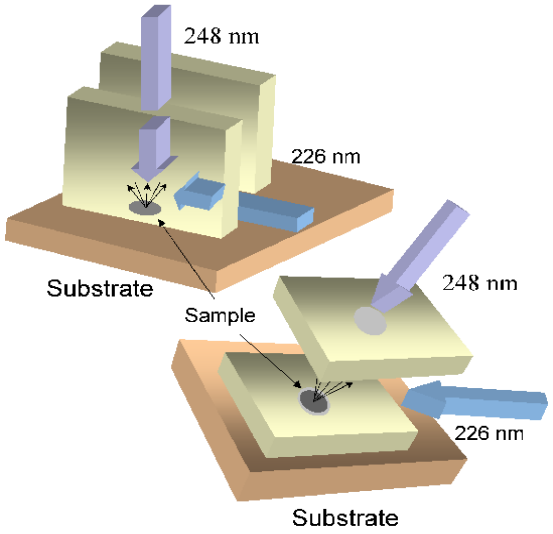

Fig. 3. Electrode-surface orientation. Top electrodes are designated VE for vertical electrodes and the bottom electrodes are designated HE for horizontal

Figure 3 depicts two sets of miniature, stainless steel electrodes that collect the ions and electrons. We denote the set depicted in the top of figure 2 as VE for vertical electrodes. They are perpendicular to the substrate surface and are approximately 15 mm x 15 mm in size with a 5-mm gap and ~0.5 mm from the surface. A 700-V bias between them results in an average electric field of ~140 V/mm. We denote the set depicted in the bottom of figure 2 as HE for horizontal electrodes. They are parallel to the substrate surface and are similar to the VE electrodes, except that they have a 6-mm gap and contain 2-mm holes for the passage of the excitation laser beam. An 850-V bias between them yields an average field of ~140 V/mm, the same as in the VE electrodes. The lower plate is insulated and is ~0.5 mm from the substrate surface. A current amplifier (Keithley 427, gain 10^6 – 10^7 V/A, time constant 0.01 ms) amplifies the electrode signal and a 125-MHz oscilloscope (Lecroy, 9400) monitors it. A personal computer records the signals from a boxcar averager (Stanford Research Systems, SR250).

We prepared thin films of RDX, HMX, CL20, and TNT by coating microscope slides with known volumes of dilute solutions of the target compound in acetone and then evaporating the solvent. SPF-FD spectra are recorded with 10-shot averaging at excitation laser wavelengths of 355, 266 and 248 nm, while scanning the probe laser at a rate of 0.00375 nm/s. The substrate is translated to replenish the film. For each LOD measurement, we use 4-10 slides with varying film thickness (surface concentration) of the

target explosive. Signal levels for the response plots are recorded at a fixed excitation laser wavelength with the probe laser set to 226.2 nm, while translating the substrate so that each laser shot samples a fresh film spot. A plot of ion signal as a function of concentration yields the response curve for each compound.

Our colleagues at the U.S. Army Research Laboratory provided us with the energetic materials. High Pressure Liquid Chromatography (HPLC) analysis of the explosives reveals an HMX purity of more than 99.9% and RDX, CL20, and TNT purities of more than 99%. A UV-visible spectrometer (Hewlett-Packard, Model 8453) with Hewlett-Packard Chemstation software records the absorbance spectra of RDX and CL20 in the wavelength region of 190 nm to 400 nm. The NO_2 (485 ppm in N_2) and NO (0.097% in Ar) gases are from Matheson Tri-Gas and Airgas, respectively.

3. RESULTS AND DISCUSSION

Figure 4 shows the SPF-FD spectra of RDX, along with a REMPI spectrum of trace NO gas, in the region of 225.8 to 227.0 nm at 298K and 1 atm using the HE ionization probe (Fig. 2, bottom). The firing between the pump and probe lasers is set to 1ms. We observe similar spectra for HMX, CL20, and TNT, and with the VE probe (Fig. 2, top), but we do not observe any signal with either probe if the photofragmentation laser is off or if there is no explosive on the substrate. The prominent spectral features of the explosives are similar to those of NO, and are attributed to NO rotational lines of the Q_1+P_{21}, P_1, and P_2+Q_{12} branches of the A-X (0,0) band (Cabalo and Sausa, 2003). The fact that the explosives yield a unique molecular fingerprint of NO is definitive proof that SPF-FD successfully detects residues of low vapor pressure explosives at ambient conditions. The overall SPF-FD mechanism involves the following steps:

$$R\text{-}NO_2\,(s) \xrightarrow{h\nu\ (uv)} R + NO\,(X^2\Pi) + O \qquad (1)$$

$$NO\,(X^2\Pi) \xrightarrow{h\nu\ (226\ nm)} NO\,(A^2\Sigma^+) \xrightarrow{h\nu\ (226\ nm)} NO^+\,(X^2\Sigma^+) + e \qquad (2)$$

in which step (1) represents the uv laser excitation of a thin energetic film that yields ground state NO, and step (2) represents the (1+1) REMPI of the NO fragment by means of its real, intermediate $A^2\Sigma^+$ state ($\tau \sim 215$ ns). We observe an enhancement in the NO ionization because the intermediate state's energy is resonant with one 226-nm photon. Steps (1) and (2) depict very efficient processes and require only a few microjoules of laser radiation. These processes are depicted in figure 5.

Our study on the effects of common laser photolysis wavelengths on the SPF-FD technique's sensitivity shows the SPF-FD signal increases with decreasing wavelength. At 248 nm the signal is approximately a factor two greater than at 266 nm, and at 355 nm no detectable signal is observed. At 10.6 μm the signal is obscured by contaminants resulting from the infrared–induced decomposition of RDX, and work at this wavelength was discontinued. RDX is consumed more rapidly at 10.6 μm compared to wavelengths in the ultraviolet because the infrared beam rapidly heats an area of the substrate greater than its size.

We also investigated the effects of delay between photolysis and ionization lasers and photolysis laser energy. The SPF-REMPI signal was monitored as a function delay between lasers in order to determine the optimal delay between the photolysis and ionization lasers. All delay times (0.1 - 40-ms) resulted in the same signal indicating that the NO concentration from RDX reaches a steady state value very quickly. A delay of 1 ms is arbitrarily selected for further study. The SPF-REMPI signal increases linearly with laser energy up to 12 μJ, and then begins to level off.

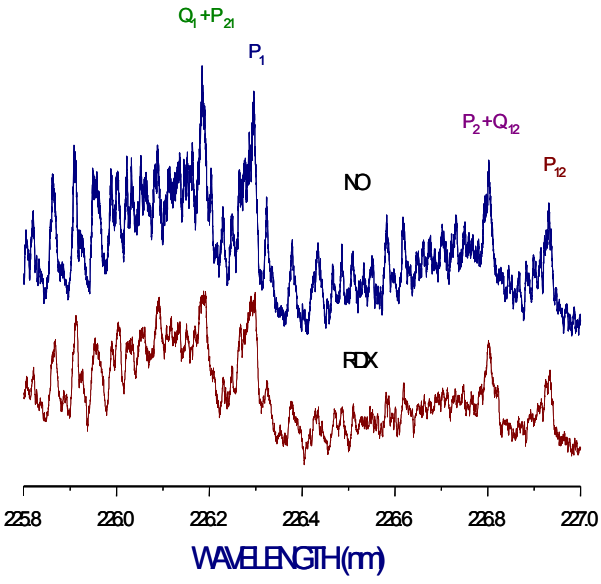

Fig. 4. RDX SPF-FD and NO REMPI Spectra

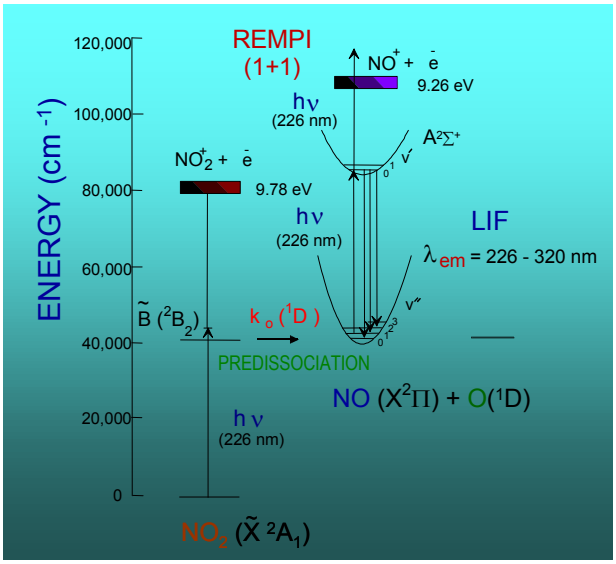

Fig. 5. NO and NO_2 potential energy diagrams

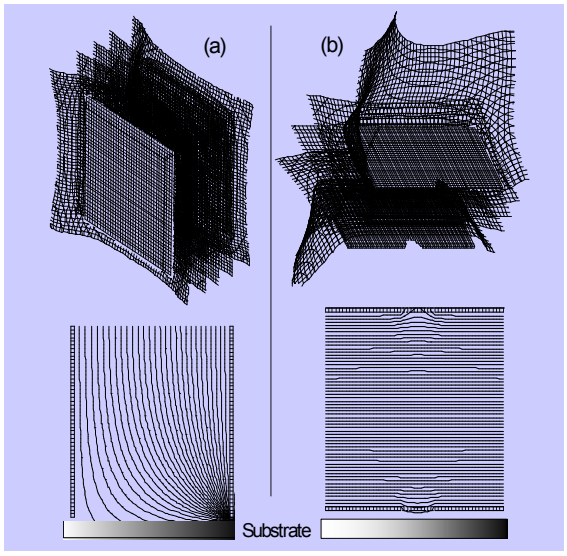

Fig. 6. Calculated equipotentials: (a) VE electrodes and (b) HE electrodes.

We determined the efficacy of both HE and VE probes by testing them on RDX during identical operating conditions (same pump and probe laser energy and wavelength). Our results show that the HE probe with horizontal electrodes is about an order of magnitude more sensitive than the VE probe with vertical electrodes. An important factor that contributes to the difference in sensitivity is the effect of the substrate on the probe's electric field. We investigated this effect with Simeon 7.0, a PC-based, electrostatic lens analysis and design program developed by David Dahl of the Idaho National Engineering and Environmental Laboratory. (Simeon was developed originally by D. C. McGilvery at Latrobe University Bundoora Victoria, Australia, 1977).

Simion calculates the electric field and scalar potential between the electrodes in the presence of a substrate by solving the Poisson Equation

$$\nabla^2 \phi = \frac{\rho}{\varepsilon}, \qquad (3)$$

in which ϕ is the electric potential, ρ is the charge distribution, and ε is the absolute permittivity. A "method of images" creates a valid solution of the electric potential by using the distribution of real charge plus "simulated" or "image" charge that is idealized to be on the other side of the plane defined by the substrate surface and that fulfills the boundary conditions. The potential for the point charge close to the substrate is a combination of the charge and its mirror "image" charge multiplied by a constant that is defined by

$$(\kappa_e - 1) / (\kappa_e + 1), \qquad (4)$$

in which κ_e is the dielectric constant in the case of a linear isotropic homogeneous dielectric.

Figure 6 shows simulations of the VE and HE probe's electric field with a dielectric substrate close to the probes. The top panels show a three-dimensional perspective of the probe's equipotential surfaces, whereas the bottom panels show a two-dimensional "slice" of the three-dimensional picture depicting the equipotential surfaces as equipotential lines. When the substrate is brought close to the edge of the VE probe, a significant component of the electric field is oriented towards the substrate surface and away from the probe, as shown by the equipotential lines (the force vectors are normal to the equipotential lines and surfaces). The electrons or ions are forced away from the probe and are not collected. In contrast, the HE probe's electric field is mostly unperturbed as the substrate approaches the electrodes, as shown in the bottom of Fig. 2B, and all the charged species are collected. Thus, the HE probe is more sensitive than the VE probe. The HE probe also offers additional advantages over the VE probe. First, it can sample metallic substrates because the high voltage electrode near the surface can be insulated, and second, it can be made to operate as a miniature ion mobility spectrometer for increased selectivity.

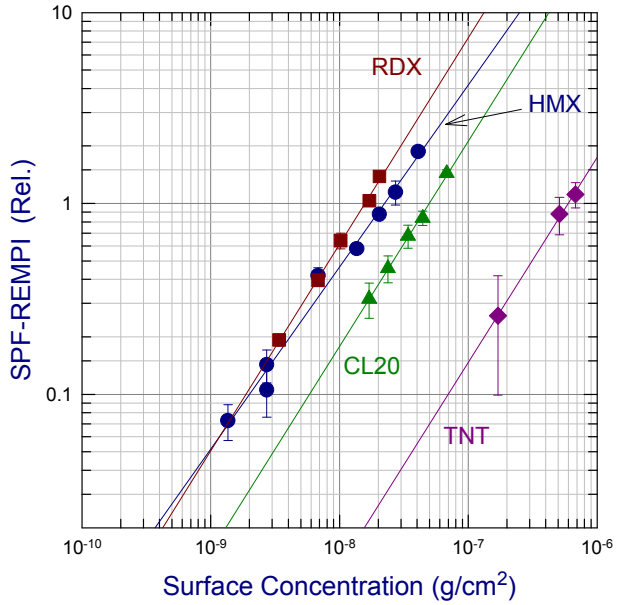

Fig 7. Response curves of the selected energetic materials

The probe's configuration and electric field orientation play a role in the extraction and collection of charged species from the laser irradiation of the energetic films. We recorded RDX signal traces with both the VE and HE electrodes at 248 nm with the 226-nm laser off. The 248-nm laser beam was normal to the VE probe's electric field but parallel to that of the HE probe. Both traces reveal the time evolution of the charged species. The curves have about the same area but different shapes. Most of the signal from the VE probe occurs in the first 50 μs, whereas the signal from the HE probe is distributed over 150 μs. We attribute the peaks to a combination of photoelectrons (t~15 μs) and molecular ions (t >15 μs). Although both probes collect the photoelectrons, the HE probe collects more of the ions. The origin and assignment of the positive ions are not well known and are the subject of future inquiry.

Figure 7 shows response curves of the various explosives at 248 and 226.3 nm for the pump and probe laser wavelength, respectively. The solid straight lines are best fits to the data, which are represented by symbols. The responses are directly proportional to the amount of material on the substrate for a fixed optical setup and laser energy. In all cases, the signal is over a wide range of concentrations. The LOD is defined by $3\sigma/R$, where R is the response and σ is the root mean square of the noise. Table 1 shows the LOD for the various energetic materials. They are 1.4 ng/cm^2 for RDX, 2.0 ng/cm^2 for HMX, 7.1 ng/cm^2 for CL20, and 15.4 ng/cm^2 for TNT. Ranking the compounds by limit of detection yields a sensitivity of RDX > HMX > CL20

Table 1. Energetic materials with their limit of detection (LOD) and extinction coefficient at 248 nm, and their R-NO_2 bond energy.

Energetic Material	LOD (ng/cm^2)	Extinction Coefficient (ε)[a] (x10^3)	R-NO2 Bond Energy (kcal/mol)
RDX	1.4	7.2, 6.8	34.2, 34.3, 39.0
HMX	2.0	9.4	38.8
CL20	7.1	15.0	39.4
TNT	15.4	13.6, 14.2	>60

[a]ε = log (Io/I)/ℓc, where Io is the intensity of the incident light, I is the intensity of the transmitted light, ℓ is the pathlength in cm, and c is the concentration in moles/liter.

TNT. The RDX value of 1.4 ng/cm^2 corresponds to ~ 0.4 fg of RDX and compares favorably to the 200-pg value obtained by Chang and coworkers (Cheng et al., 1995). Table 1 shows that the LOD ratio of TNT to RDX is ~11. This value is similar to the value of 10 obtained by our group by one-laser PF-FD of gaseous RDX and TNT at 226 nm near ambient conditions (Swayanbunathan et al., 1999). Probing the NO fragment by REMPI yielded TNT and RDX LODs of 70 and 7 ppb, respectively.

The overall SPF-FD mechanism represented in steps (1) and (2) suggests that the LOD for each energetic material depends on the amount of NO produced at 248 nm, step (1), and the amount of NO detected at 226.3 nm, step (2). In our LOD measurements, the probe energy and optical setup are the same for all the compounds; thus, the amount of NO produced at 248 nm depends on the absorption coefficient of the target compound at 248 nm and the governing mechanism that produces NO. Table 1 lists the 248-nm extinction coefficients of the energetic materials studied. The RDX and CL20 values from this work are 7.6x10^3 and 1.5x10^4, respectively. The RDX, HMX and TNT values of 6.8x10^3, 9.4x10^3, and 13.6x10^3 are interpolated values from extinction coefficient curves of Scroeder and coworkers (Scroeder et al., 1951), whereas that of TNT, 14.2x10^3, is obtained from the work of Kamlet, Hoffsomer, and Adolph (Kamlet et al., 1962). All of the RDX values, as well as the TNT

values are in good agreement considering the error in interpolation at 248 nm. Ordering the compounds by absorbance at 248 nm yields CL20 > TNT > HMX > RDX. *A priori,* we expect the compounds' LOD order to parallel their absorbance order. Surprisingly, this is not the case: the CL20 and TNT extinction coefficients are higher than those of RDX and HMX, yet their sensitivities are lower. Also, the extinction coefficient of CL20 is about the same as that of TNT, but its sensitivity is almost twice that of TNT. Clearly, the molecule's absorption at 248 nm plays less of a role in its LOD than the mechanism for generating NO.

The mechanisms involved in the 248-nm laser-irradiation of RDX, CL20, HMX and TNT on surfaces are complex. They may include photothermal and photochemical processes, as well as surface effects. Among the many suggested initial steps in the thermal decomposition of the selected energetic materials in the condensed-phase, the most likely mechanism is the homolysis of the nitro functional group, which is weakly attached to the remainder of the molecule. NO_2 may then react further to produce NO. Table 1 also lists the R–NO_2 bond dissociation energy for the four compounds (Wu and Fried, 1997, Kuklja and Kunz, 2001, Chakraborty et al., 2001, Rice, 2004, private communication, and Gonzalez et al., 1985). Table 1 shows that TNT has the highest bond dissociation energy for R–NO_2 scission by at least 20 kcal/mol. In part, this is because the NO_2 group in TNT is bonded to a carbon-atom containing ring that is more stable than the nitrogen-atom containing ring in the nitramines, RDX, HMX, and CL20. Thus, TNT releases its NO_2 less readily than RDX, HMX, and CL20, and its LOD value is expected to be larger than that of the nitramines. Also, TNT has several alternative decomposition pathways that compete with R–NO_2 bond scission. They include nitro/nitrite isomerization (Gonzalez et al., 1985), oxidation of $-CH_3$ to form anthranil (He et al., 1988), and catalysis. These pathways also decrease the initial production of NO_2 and contribute to TNT's lower sensitivity relative to the nitramines.

The R–NO_2 bond dissociation energy of nitramines RDX, HMX, and CL20 is similar, around 34 to 39 kcal/mol. However, CL20 has an LOD that is a factor of nearly 3 times greater than that of RDX and HMX. This suggests that the process of NO_2 release in these molecules is more complicated than the simple cleavage of a single nitro functional group and may involve the loss of more than one nitro group from each molecule. In the case of RDX and HMX, the energy for the ring's C—N bond cleavage is lowered after the removal of the nitro functional group, and further decomposition generating additional NO_2 is possible (Patil and Brill, 1991). In contrast, the C—N bond in CL20's backbone is stabilized following NO_2 homolysis, and further decomposition is hindered (Patil and Brill, 1991, and Geetha et al., 2003). The backbone of RDX and HMX is two-dimensional, and it is sterically difficult for the radical site to stabilize itself by interacting with its other parts. In the case of CL20, its cage structure promotes the stabilization of the radical site by rearrangement or multiple bond formation with other parts of the backbone and prevents additional NO_2 loss. Although our argument for CL20's LOD being larger than that of RDX and HMX is plausible, other governing processes may be operable.

Figure 8 shows a SPF-FD spectrum of NO from RDX using the HE probe, along with a spectral simulation of NO, in the region of 225.8 to 226.8 nm. Both spectra reveal NO rotational lines of the Q_1+P_{21}, R_1+Q_{21}, Q_2+R_{12}, R_2, and R_{21} branches of the A-X (0,0) band. A multiparameter computer program based on a Boltzmann rotational distribution analysis generates the simulation spectrum (Cabalo and Sausa, 2003). Parameters include laser line shape, rotational line strengths and energies, and temperature. The best fit of the data using a Gaussian function for the laser line shape yields a rotational temperature, T_R, of 304 ± 10 K, and indicates that the NO fragment is thermally equilibrated by collisions with O_2 and N_2 in the time scale of the experiment, as expected from gas kinetic calculations.

We also probed the NO fragment for vibrational excitation and determined its vibrational temperature. Laser radiation near 226 nm excites the NO A-X (0,0) transitions and probes the NO $X^2\Pi$ (v"=0) state, whereas laser radiation near 224 and 237 nm excites the (1,1) and (0,1) transitions, respectively, and probes the (v"=1) state. We observed significant

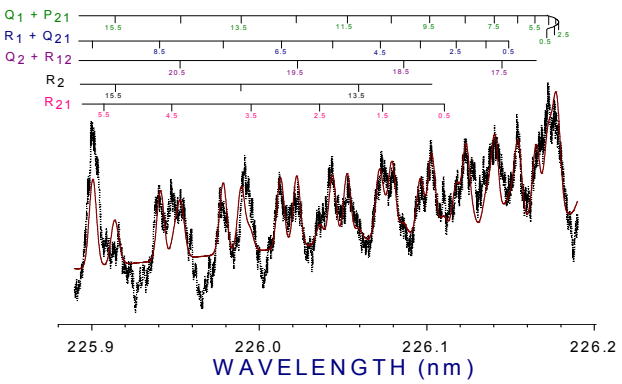

Fig. 8. Results of rotational analysis: best fit of the SPF-FD signal from RDX.

signal from all the energetic materials at 226 nm, but little, if any, at 224 nm or from RDX at 237 nm. This indicates that NO is formed primarily in its $X^2\Pi$ (v"=0) state with a vibrational temperature, T_v, of ~298K. The millisecond time of our experiment is sufficient to vibrationally relax NO, which requires a few microseconds. Heflinger and coworkers observed vibrationally excited NO $X^2\Pi$ (v"=2) from the 248-nm photolysis of TNT vapor near ambient conditions (Arusi-Parpar et al., 2001). This is not suprising because the time between the TNT photolysis and subsequent LIF detection of NO (~ 10 ns) is less than the time required for NO to vibrationally relax. Also, TNT experiences fewer collisions when it decomposes in the gas phase compared to the condensed phase.

Unlike the 224-nm excitation of the energetic films, we observe a significant NO $X^2\Pi$ (v"=1) signal when we photolyze NO_2 gas at 224 nm. In this case, the time between the photolysis of NO_2 and ionization of NO (~6 ns) is insufficient to vibrationally thermalize NO. We do not observe any v"=1 signal from room temperature NO, as expected, because its Boltzmann, (v"=1/v"=0) ratio is $\sim 10^{-5}$ at 298K. We calculate an NO_2 detection limit of ~ 150 ppb at 224 nm from this and prior work (Pastel and Sausa, 2000). This suggests that less than 150 ppb of NO_2 from the energetic film survives ~1 ms after the laser excitation pulse. Thus, the NO signal from the energetic films results probably from secondary reactions of NO_2 rather than the gas-phase photolysis of NO_2 emanating from the energetic film. Brill and coworkers show that NO_2 is the primary product from the rapid heating of CL20 (Gongwer and Brill, 1998) and RDX and HMX (Oyumi and Brill, 1985). They observe that NO, if present at all in the early stages of the decomposition, increases rapidly as NO_2 reduces from secondary reactions. Geetha and coworkers corroborate these observations from their work on the thermal decomposition of CL20 (Geetha et al., 2003).

CONCLUSION

We have presented a new technique coined SPF-FD for detecting explosive residues. The technique uses an ultraviolet laser to photolyze the energetic materials and a second 226-nm laser to ionize the resulting NO photofragment. We have demonstrated is analytical utility on trace concentrations of RDX, HMX, CL20, and TNT energy at atmospheric pressure and room temperature with LODs in the low ng/cm^2 range using a few microjoules of laser. Maximum signal is observed at 248 nm, over 266 and 355 nm, where the absorption coefficient of the explosives is the strongest. Our HE probe is a factor of ~ 10 more sensitive than our VE probe because the substrate perturbs the electric field of the HE probe less than that of the VE probe, as shown in our ion optics calculations.

The sensitivity of the SPF-FD technique also depends on the photochemical and photothermal processes yielding NO. NO is rotationally and vibrationally equilibrated in the time scale of our experiment and is formed probably from secondary reaction of NO_2. TNT and CL20 have lower sensitivities than RDX and HMX, whose sensitivities are comparable. TNT's stronger R-NO_2 bond compared to that in the nitramines and decomposition pathways that compete with R-NO_2 homolysis might contribute to its low sensitivity. In the case of CL20, whose R-NO_2 bond strength is comparable to that of RDX and HMX, its cage structure likely inhibits the escape of additional NO_2 groups, after primary R-NO_2 homolysis, and contributes to its low sensitivity.

In short, our SPF-FD approach exhibits great potential for detecting trace energetic materials on surfaces in real time and *in situ* because of its high sensitivity and simplicity of instrumentation. It is not restricted to explosives and its application to chemical warfare agents and other hazardous materials is ongoing.

ACKNOWLEDGEMENTS

We thank Dr. B. Rice of the US Army Research Laboratory (ARL) for calculating the N-NO_2 bond energy in CL20, Drs. R. Pesce-Rodriguez and P. Kaste of ARL for the energetic material samples, and Drs. A. Kotlar and M. Schroeder of ARL for many helpful discussions. We also thank the National Research Council Postdoctoral Research Associateship Program (J. Cabalo) and the ARL Director's Research Initiative for support (R. Sausa).

REFERENCES

Arusi-Parpar, T., Heflinger, D. and Lavi, R., 2001: Photodissociation Followed by Laser-Induced Fluorescence at Atmospheric Pressure and 24 Degrees C: A Unique Scheme for Remote Detection of TNT, *Applied Optics* **40 (36)**, 6677-6681.

Cabalo, J. and Sausa, R., 2003: Detection of Hexahydro-1,3,5-trinitro-1,3,5-triazine (RDX) by Laser Surface Photofragmentation- Fragment Detection Spectroscopy," *Appl. Spectroscopy* **57(9),** 1196-1199, and references therein.

Chakraborty, D., Muller, R.P., Dasgupta, S. and W.A. Goddard III, W.A., 2001: Mechanism for Unimolecular Decomposition of HMX (1,3,5,7-

tetranitro-1,3,5,7-tetrazocine), An Ab Initio Study, *J. Phys. Chem.* A **105(8),** 1302-1314.

Cheng, C., Kirkbridge, T.E., Batchelder, D.N., Lacey, R.J. and Sheldon, T.G., 1995: In-Situ Detection and Identification of Trace Explosives by Raman Microscopy," *Journal of Forensic Sciences* **40**31 -37.

Geetha, M., Nair, U.R., Sarwade, D.B., Gore, G.M., Asthana, S.N. and Singh, H., 2003: Studies on CL20: The Most Powerful High Energy Material," *Journal of Thermal Analysis and Calorimetry* **73**, 913-922.

Gongwer, P.E. and Brill, T.B., 1998: Thermal Decomposition of Energetic Materials 73. The Identity and Temperature Dependence of "Minor" Products From Flash-Heated RDX," *Combustion and Flame* **115 (3)**, 417 423.

Gonzalez, A.C., Larson, C.W., McMillen, D.F. and Golden, D.M., 1985: Mechanism of Decomposition of Nitroaromatics- Laser-Powered Homogeneous Pyrolysis of Substituted Nitrobenzenes," *J. Phys. Chem*. **89(22)**, 4809-4814.

He, Y.Z., Cui, J.P., Mallard, W.G. and Tsang, W., 1988: Homogeneous Gas-Phase Formation and Destruction of Anthranil from o-nitrotoluene Decomposition, J. *Am. Chem. Soc.* **110(12)**, 3754 –3759.

Kamlet, M.J., Hoffsommer, J.C. and Adolph, H.G., 1962: Steric Enhancement of Resonance. I. Absorption Spectra of the Alkyltrinitrobenzenes," Journal of the American Chemical Society **84(20**), 3925-3828.

Kuklja, M.M. and Kunz, A.B., 2001: Electronic Structure of Molecular Crystals Containing Edge Dislocations," *Journal of Applied Physics* **89 (9),** 4962-4970.

Oyumi, Y. and Brill, T.B., 1985: Thermal-Decomposition of Energetic Materials 3. A High-Rate, In Situ, FTIR Study of the Thermolysis of RDX and HMX with Pressure and Heating Rate as Variables," *Combustion and Flame* **62 (3)**, 213-224.

Pastel, R.L. Sausa, R.C., 2000: Spectral Differentiation of Trace Concentrations of NO_2 from NO by Laser Photofragmentation with Fragment Ionization at 226 and 452 nm: Quantitative Analysis of NO-NO_2 Mixtures," *Applied Optics* **39(15),** 2487-2495.

Patil, D.G. and Brill, T.B., 1991: Thermal Decomposition of Energetic Materials 53. Kinetics and Mechanisms of Thermolysis of Hexanitrohexazaisowurtzitane," C*ombustion and Flame* **87**, 145-151.

Scroeder, W.A., Wilcox, P.E., Trueblood, K.N. and Dekker, A.O.,: 1951: Ultraviolet and Visible Absorption Spectra in Ethyl Alcohol: Data for Certain Nitric Esters, Nitramines, Nitroalkylbenzenes, and Derivatives of Phenol, Aniline, Urea, Carbamic Acid, Diphenylamine, Carbazole, and Triphenylamine," *Analytical Chemistry* **23(12)**, 1740-1747. SIMION, 2004:

Swayambunathan, V., Singh, G. Sausa, R., 1999: Laser Photofragmentation-Fragment Detection and Pyrolysis-Laser-Induced Fluorescence Studies on Energetic Materials," *Appl. Optics* **38(30)**, 6447-6454..

Wu, C.J. and Fried, L.E., 1977: Ab Initio Study of RDX Decomposition Mechanisms," *J. Phys. Chem. A* **101**, 8675-8679 (1997).